ORIGINAL RESEARCH ARTICLE

Probing Sulfur Vacancies in CVD-Grown Monolayer MoS$_2$ on SiO$_2$/Si in the Temperature Range 750–900°C

Rupika Tomar[1] · Bo Hsu[1] · Alejandro Perez[1] · Michael Stroscio[1,2] · Mitra Dutta[1,2]

Abstract

This work reports morphologically alike, high-quality monolayer MoS$_2$ flakes with a similar strain at various growth temperatures (750–900°C) achieved by adjusting sulfur temperature. The growth dynamics of MoS$_2$ are correlated with changes in the photoluminescence (PL) and Raman peak positions. Monolayer MoS$_2$ crystals are synthesized at different growth temperatures from 750°C to 900°C using chemical vapor deposition (CVD). We examined the structural quality and aimed to extract the recombination mechanisms in MoS$_2$ using low-temperature, variable, and low-laser-intensity PL measurements. Our studies of the defect-associated bound exciton emission are well correlated with the blueshift in the A$_{1g}$ mode of Raman spectra, blueshift in PL spectra, and x-ray photoelectron spectroscopy results for crystal grown at 900°C. Our research findings not only shed light on a thorough, non-intrusive method for modifying growth parameters to enhance optical performance, but they also suggest a way to modify the optical characteristics of MoS$_2$ while maintaining the morphology.

Keywords MoS$_2$ · chemical vapor deposition · sulfur vacancies · bound exciton · photoluminescence · defect

Introduction

Beyond graphene, the discovery of two-dimensional (2D) materials, particularly transition-metal dichalcogenides (TMDC),[1,2] has widened the scope of research into 2D materials. For their potential use in low-dimensional electrical and optical devices in a range of sectors, such as optoelectronics,[1–6] catalysts,[7] sensors,[7] memory cell[8] and field effect transistors,[9] monolayer TMDCs such as MoS$_2$, WS$_2$, and WSe$_2$ have gained considerable attention in recent years. These layered materials differ from their bulk counterparts in several ways. The bulk equivalent of MoS$_2$ has an indirect bandgap of 1.29 eV,[10] whereas monolayer MoS$_2$ has a direct bandgap of 1.9 eV.[10] Because of the inversion symmetry breaking that occurs when a monolayer of MoS$_2$ is separated from a bulk crystal, the bandgap shifts from indirect to direct, increasing the optical bandgap (for example, from 1.29 eV for bulk MoS$_2$ to 1.9 eV for monolayer MoS$_2$) due to

the significantly enhanced Coulomb interaction.[10] The substantial exciton- and trion-binding energies,[11] inversion symmetry breaking with spin-orbital coupling,[12] and valley Hall effect[13] of MoS$_2$ opens exciting potential in next-generation nanoelectronics and photonics applications.[13]

Through powerful spectroscopic techniques such as Raman and PL spectroscopy, electronic and vibrational properties of 2D flakes[14,15] are quantified efficiently. Raman spectroscopy is a non-destructive technique that has been widely used to examine 2D material layer counts, twist angles between layers, edge qualities and kinds, and the impacts of perturbations such as strain, doping, and magnetic and electric fields. MoS$_2$ exhibits two IR-active modes and four Raman-active modes[15] (E$^1_{2g}$, E$^2_{2g}$, A$_{1g}$, and E$_{1g}$) (A$_{2u}$ and E$_{1u}$). While the A$_{1g}$ mode is attributed to the out-of-plane vibration[15] of just one S atom in opposite directions, the in-plane mode E$^1_{2g}$ is produced by the opposite vibration of two S atoms with respect to the Mo between them. The in-plane covalent bonding is robust in these materials, whereas the interlayer van der Waals interaction is weak. As the layer number increases, in-plane mode is believed to be affected by the long-range interlayer coulombic interaction between molybdenum atoms[15] due to the increase in the dielectric tensor. On the contrary, the out-of-plane mode is found to be more sensitive to adsorbates on the MoS$_2$ surface and

✉ Rupika Tomar
    rtomar3@uic.edu

1   Department of Electrical and Computer Engineering, University of Illinois at Chicago, Chicago, USA

2   Department of Bioengineering, University of Illinois at Chicago, Chicago 60607, USA

electron doping.[16,17] As MoS$_2$ is reduced from a multi-layer to a monolayer, a direct bandgap excitonic transition is seen to significantly increase quantum yield. However, factors including crystal structure, local doping, and strain are likely to have an impact on the PL signal's intensities and peak positions. Recent discoveries have shown that strain can play a vital role in modulating the bandgap of TMDCs.[16–26] Additionally, the electrical band structure and mobility of 2D layers have been influenced by substrate-induced effects.[27,28] The strain and charge doping in 2D materials shift its phonon modes, and these shifts are due to the anharmonicity of molecular potentials, which can be probed by micro-Raman spectroscopy.[28] The mechanical strain[28] is shown to perturb the band structure of MoS$_2$ and carrier effective mass. Since the in-plane E$^1_{2g}$ mode is sensitive to strain,[28] thus, on applying compressive or tensile strain, the E$^1_{2g}$ mode either blue or red shifts, whereas the out-of-plane mode A$_{1g}$ remains constant. Shifts in the E$^1_{2g}$ and A$_{1g}$ modes are seen in substrates such as sapphire, mica, and SiO$_2$, which is a sign of strain and charge doping from the underlying substrates. Further, the A$_{1g}$ phonons with atomic displacements parallel to the c axis are involved in controlling the mobility of the carriers.[29]

The transport and optical characteristics of the host material are greatly influenced by electrons, holes, and excitons. Lattice point defects such as vacancies and interstitials in semiconductors can function as very effective traps for these particles.[30] If excitons attached to defects combine again radiatively, light is emitted at energies below the optical band transition energy. Because of the electron wave function's more precise localization, these interactions are stronger in decreased dimensions. In the past, vacancy defects in pristine MoS$_2$ have been introduced and controlled by electron irradiation,[9,30] thermal annealing[30] or ion-beam irradiation.[31] The most effective approach for producing high-quality,

large-scale films or crystals is chemical vapor deposition (CVD)[32]; however, because chalcogens are highly volatile, as-grown crystals are susceptible to sulfur deficiencies[33] or anionic vacancies. These sulfur vacancies act as scattering centers and, therefore, are found to degrade the device performance by lowering the mobility. However, they act as adsorbing sites that are exploited to improve the HER catalytic performance.[34] Currently, to the best of our knowledge, the growth of MoS$_2$ is most often reported at lower growth temperature (700–800°C), while the morphology varies depending on growth temperatures. In this work, we have achieved morphologically similar, high-quality monolayer flakes with similar strain at different growth temperatures (750–900°C) by tuning the sulfur temperature. The as-grown crystals are observed to have varying sulfur vacancies. The variations in PL and Raman peak positions are correlated with the growth dynamics of MoS$_2$. Additionally, the quality of the crystals grown at different temperatures is analyzed by low temperature and varied laser intensity PL measurements.

Experimental Section

Growth Setup

In this study, utilizing solid sulfur powder and molybdenum trioxide (MoO$_3$) as precursors, we synthesize monolayer MoS$_2$ films at 750°C, 800°C, 850°C, and 900°C in 20 min. With an additional S (sulfur powder) heating source upstream through a heating tape, a single-zone horizontal tube furnace (Fig. 1a) is employed to generate the monolayer MoS$_2$ directly on SiO$_2$/Si substrate. Approximately 200 mg of sulfur-containing quartz is added upstream, while the heating zone's core contained SiO$_2$/Si, Si substrates and 10 mg of MoO$_3$ powder. SiO$_2$/Si substrate (1.5 cm × 1 cm)
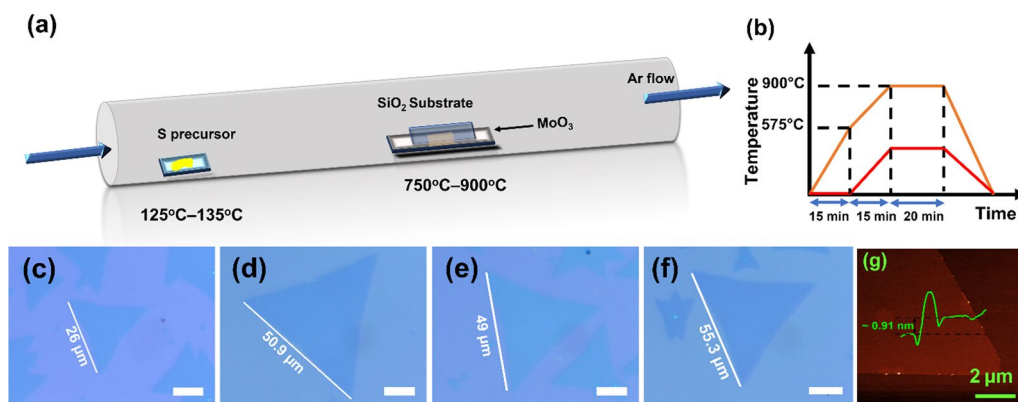

Fig. 1 (a) Experimental setup for the chemical vapor deposition (CVD) growth of single-layer MoS$_2$ on SiO$_2$/Si. MoO$_3$ is placed inside the heating zone of a furnace and sandwiched between Si and SiO$_2$/Si, while sulfur is loaded upstream outside the furnace and heated separately. (b) Growth (orange) and sulfur (red) heating profile. (c)–(f) Optical images of MoS$_2$ at 750°C, 800°C, 850°C and 900°C, respectively. All scale bars are 10 μm. (g) Atomic force microscopy (AFM) images of MoS$_2$ grains.

is cleaned with acetone, IPA (isopropyl alcohol), and DI water before being placed on top of the MoO_3 powder with a spacing of approximately 0.5 mm. To reduce the oxygen content and eliminate any remaining impurities, the tube is then purged with argon for 30 min and then pumped down to a pressure of 0.667 kPa. The heating process that corresponds to the temperature at the furnace's center begins with a slow ramping rate of between 11°C and 22°C per min, depending on the temperature set point for the chamber. This is followed by a gradual heating from room temperature to 575°C at a rate of about 30°C per min. The furnace's temperature is maintained at 750°C, 800°C, 850°C, and 900°C for 20 min before naturally cooling to ambient temperature. Sulfur begins to slowly evaporate at a temperature near 575°C (Fig. 1b) in the furnace's center and is held at growth temperatures for the same period. The entire growing procedure is carried out with 100 sccm argon. The sulfur heating temperature is adjusted with the growth temperature to obtain similar morphology (see supplementary Table SI).
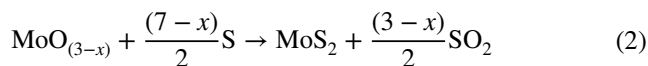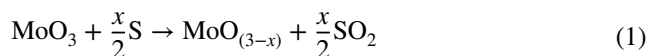
Characterization

A Keyence VHX-6000 microscope is used to capture the MoS₂ optical microscope (OM) images. Renishaw inVia Reflex Raman and PL spectroscopy are utilized to examine the structural and optical characteristics of as-grown MoS₂ grains at room and low temperatures. The 532 nm line of a solid-state laser is used to excite the samples, and a 50X objective is used to focus the laser beam. For the Raman (PL) measurements, 1.57 mW of laser power and 1800 lines/m of grating are utilized, respectively. An atomic force microscope (Bruker Nano AFM) in ScanAssyst mode is used to examine the surface topography of the grains. A Thermo Scientific ESCALAB 250Xi is used to conduct x-ray photoelectron spectroscopic investigations with an Al-Ka (1486.6 eV) x-ray source.

Results and Discussion

MoO_3 is first transformed to molecular clusters[35] during the growth process, which is followed by condensing of these molecular clusters into MoO_{3-x} suboxide nanoparticles under the influence of sulfur vapors at 575°C. Suboxide nanoparticles are then sulfurized to produce monolayer or few-layered MoS₂.[36] The dynamics of the growth process are greatly influenced by sulfur vapor concentration. The generation of suboxide or oxi-chalcogenide particles with an orthorhombic crystal structure is initiated by the weak sulfur environment.[37]

The strong sulfur environment stems from the formation of transition-metal fullerenes, while a moderately reducing

environment results in a TMDC monolayer.[36,37] Therefore, it becomes crucial to optimize the sulfur temperature in relation to the growth temperature. Experimentally, it has been found that the relatively stronger sulfur environment with respect to the growth temperature yields continuous film of MoS₂ instead of triangular domains. The reaction is possibly occurred in the following steps[38]:

$$MoO_3 + \frac{x}{2}S \rightarrow MoO_{(3-x)} + \frac{x}{2}SO_2 \tag{1}$$

$$MoO_{(3-x)} + \frac{(7-x)}{2}S \rightarrow MoS_2 + \frac{(3-x)}{2}SO_2 \tag{2}$$

At substrate regions directly above the precursor, the vapor flux is greatest. The concentration of MoO_{3-x} varies over the substrate's length. Because of the high precursor ratio in the center of the substrate, there is a mixture of continuous film and large flakes of around 50 μm to 70 μm. At the downstream end of the substrate, comparatively smaller flakes of around 10–30 μm are observed (see supplementary Figure S1). The increase in growth temperature results in the increase of domain size. At lower growth temperature, fewer active mobile species are produced due to the low sublimation rate of precursors. Since the diffusion rate is low at lower growth temperatures, the grain size obtained is comparatively small. Increase in temperature accelerates the diffusion of mobile species and thus larger grains are produced. Additionally, it is discovered that when the growth temperature increases, the nucleation density decreases. Our findings are consistent with the nucleation model of the vapor phase deposition proposed by Burton and Cabrera, which states that the nucleation probability is inversely related to substrate temperature and inversely proportional to supersaturation.[39] The optical mapping of CVD-grown MoS₂ shows uniform flake color in Fig. 1c–f, indicating that the crystals are free from grain boundaries and adlayers. Each grain's step height is 0.91 nm (Fig. 1g), further confirming the growth of a monolayer MoS₂.[27]

Raman and PL spectroscopy are utilized to collect lattice vibrations and excitonic (electron–hole pair generation) properties, respectively, of MoS₂ grown by CVD. The Raman mapping of MoS₂ grains at all growth temperatures is presented in supplementary Figure S2 and reveals that the as-grown crystals exhibit uniform crystallinity and spatial uniformity. The Raman spectra of MoS₂ grains grown at different temperatures are displayed in Fig. 2a. The E^1_{2g} peak which is attributed to the vibration of the Mo-S bond in the in-plane direction is found at 382.55 cm⁻¹ for the crystals grown at different temperatures. From the Raman spectra obtained in Fig. 2a, the change in wavenumber is plotted with respect to the growth temperatures in Fig. 2b. It is shown in Fig. 2b that the A_{1g} mode (attributed to the vibration of the Mo-S bond in the out-of-plane direction) for
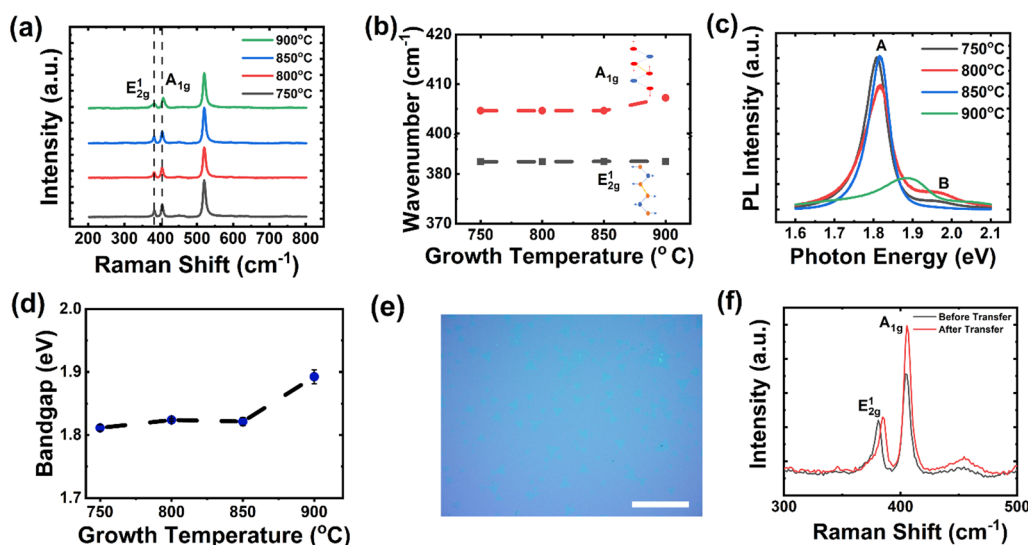
Fig. 2 (a) Raman spectra for MoS_2 grains at growth temperatures 750°C, 800°C, 850°C and 900°C, respectively. (b) Change in wavenumber of the A_{1g} mode and E^1_{2g} mode with respect to growth temperatures. (c) Photoluminescence spectra for MoS_2 grains at growth temperatures 750°C, 800°C, 850°C and 900°C, respectively. (d) Change in bandgap of as-grown MoS_2 grains with respect to the growth temperatures. (e) Optical image of flakes after wet transfer. Scale is 100 μm. (f) Comparison of Raman spectra before and after wet transfer.

growth temperatures 750°C, 800°C, and 850°C (shown by the red dotted line) is found at 404.62 cm^{-1} while for crystals grown at 900°C, this mode is found at 407.21 cm^{-1}, and thus it is up-shifted by 2.6 cm^{-1}, while the E^1_{2g} mode (shown by the black dotted line) remains constant at 382.55 cm^{-1}. We observe a strong PL emission peak (Fig. 2c) around 1.81–1.83 eV for grains grown at 750°C, 800°C, and 850°C respectively, and a weaker emission peak around 1.89 eV. However, for a growth temperature of 900°C, the PL peak shows a blueshift to 1.87–1.91 eV (Fig. 2d). The two bands, A and B, have been classified as direct excitonic transitions as a result of the valence band's spin–orbit splitting. The relative strengths of the A and B emission features in our samples are a sign of a high-quality monolayer sample.[40] Furthermore, the PL emission from the MoS_2 grains grown at 750°C, 800°C, and 850°C is found to be enhanced around six- to sevenfold compared to the emission intensity of the MoS_2 grains grown at 900°C.

It has been well established that both strain and charge doping[41–43] have an impact on the optical bandgap modulation of MoS_2. MoS_2 bandgap has been found to increase due to compressive strain (i.e., PL blueshift, E^1_{2g} mode blueshift), and tensile strain decreases the bandgap (i.e., PL redshift, E^1_{2g} mode redshift),[44] while the A_{1g} mode remains constant. To investigate the presence of strain, the Raman measurements are recorded before and after the wet transfer of flakes. The optical mapping in Fig. 2e shows the clean transfer of the grown flakes to the other SiO_2 substrate. It is observed that after the transfer there is a blueshift of 4 cm^{-1} in the E^1_{2g} mode (Fig. 2f), indicative of tensile strain present

in our grown samples. The Raman spectra of the as-grown samples in Fig. 2a show that the E peak is constant for all growth temperatures, thus indicating that there is some strain present at all growth temperatures. As a result, the strain cannot explain the observed blueshift. To clarify the cause of the PL blueshift seen in our sample, measurements at low laser and varied intensities are performed to extract the information about the recombination mechanism and presence of defects.

High excitation power intensities are predicted to cause the PL intensity of the bound exciton (X_b) to saturate when its associated defects are present.[45] Bound excitons (X_b) are associated with the defects present in the crystals. An e–h pair bound to a defect is usually the cause of an additional energy lower than the bandgap energy (free neutral excitons, X_O). Therefore, at low laser excitation, the bound exciton peak is enhanced. Defect peak intensity as a function of excitation power dependence is shown in Fig. 3a. At 900°C growth temperature, there is a defect origin peak indicating the presence of defects. The intensity of the bound exciton peak is found to be pronounced for the 900°C growth temperature. To further confirm the presence of defects and extract information on the recombination mechanism at the highest growth temperature, PL spectra are recorded at different laser intensities (Fig. 3b–h, supplementary Figure S3). The luminescence intensity I of PL emission lines is reported to be proportional to P^k, where P is the power of the exciting laser radiation and k has a value of $1 < k < 2$ for band-to-band transition and $k < 1$ for transitions caused by defects and donors/acceptors.[46] The plot of PL intensity area

under the curve[46] with respect to different excitation power is shown in the insets in Fig. 3b–h. It is a nearly linear plot with a positive slope, which improves linearly from 750°C to 850°C growth temperature, thus showing that the recombination is mainly direct band-to-band radiative, and then decreases (Fig. 3j) for 900°C growth temperature, implying the presence of defect states.[46]

We further assess the optical quality of the as-grown MoS₂ crystals by performing low-temperature PL measurements (Fig. 4a–d). The disparities in PL intensities of MoS₂ grown at different temperatures are easier to understand once the defects in MoS₂ have been identified. The PL quantum efficiency is as follows:
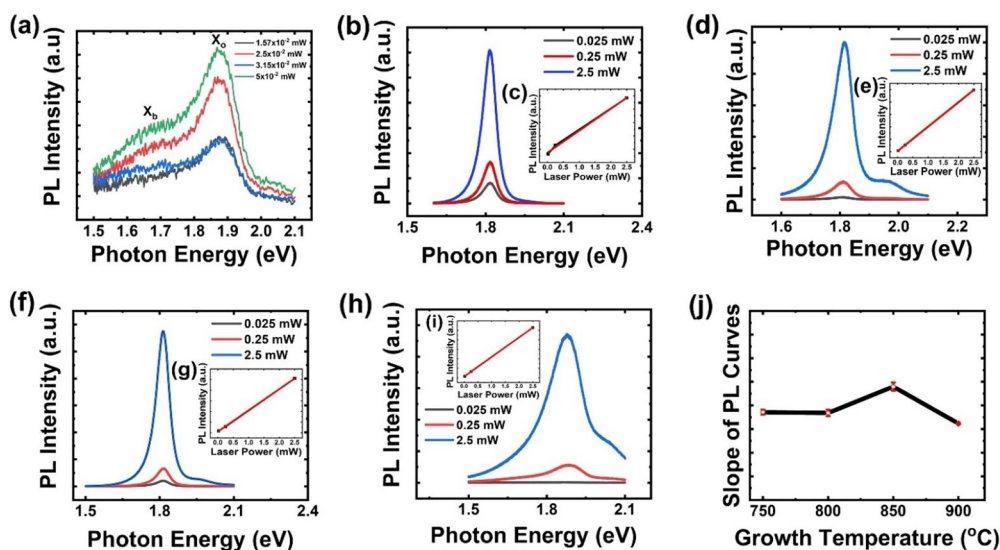
Fig. 3 (a) PL intensity of bound excitons (X_b) and free excitons (X_o) as a function of excitation laser power for crystal grown at 900°C. PL spectra at different laser excitation power as a function of photon energy for (b) crystals grown at 750°C, inset. (c) PL intensity area variation vs. different laser excitation. (d) Crystals grown at 800°C, inset. (e) PL intensity area variation vs. different laser excitation. (f) Crystals grown at 850°C, inset. (g) PL intensity area variation vs. different laser excitation. (h) Crystals grown at 900°C, inset. (i) PL intensity area variation vs. different laser excitation. (j) Slope of PL curves (obtained from linear fitting of the data points collected at different laser power) measured for all growth temperatures.
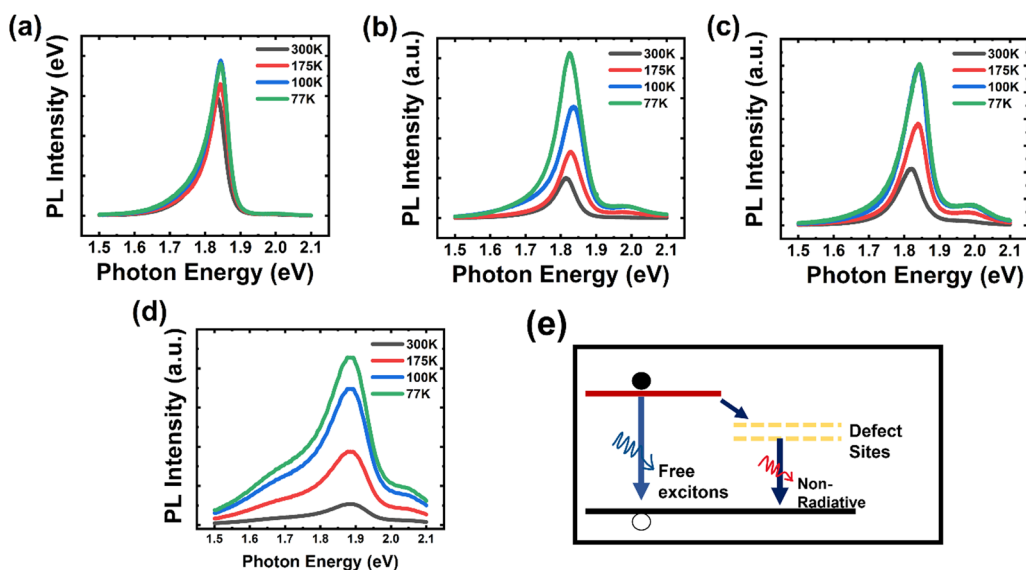

Fig. 4 PL spectra measured over the temperature range from 77 to 300 K of a MoS₂ monolayer grown at (a) 750°C, (b) 800°C, (c) 850°C, and (d) 900°C, respectively, (e) Recombination pathways for electrons in the presence of defects.
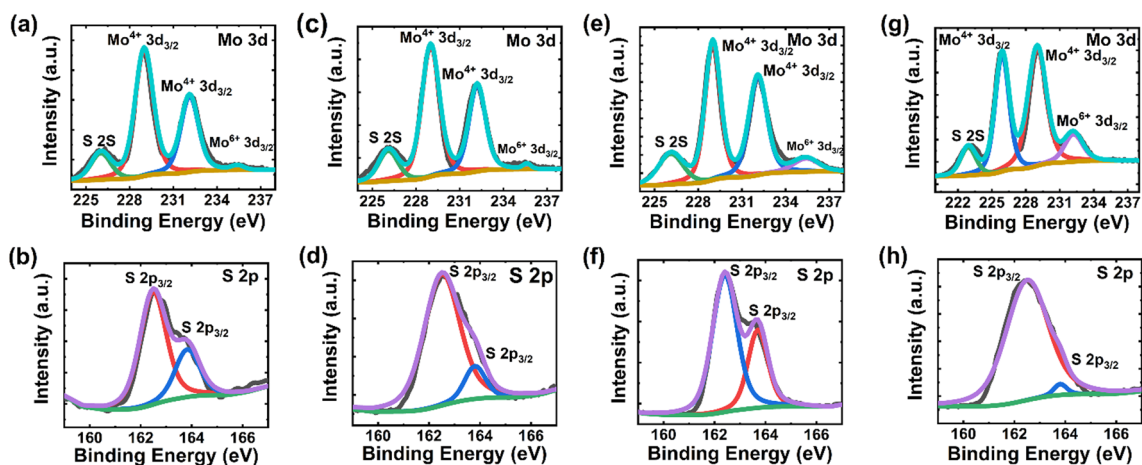
Fig. 5 X-ray photoelectron spectroscopy (XPS) core level spectra of Mo 3d and S 2p of MoS$_2$ grown at 750°C (a and b), 800°C (c and d), 850°C (e and f), and 900°C (g and h).

$$\eta = \frac{k_x}{k_x + k_{nx}} \quad (3)$$

$$k_{nx} = k_{defect} + k_{relax} + k_{other} \quad (4)$$

where radiative and non-radiative recombination rates are k_x and k_{nx}, respectively; the non-radiative recombination caused by a defect is represented by k_{defect}[47]; the electron relaxation in the conduction and valence bands is represented by k_{relax}; and other non-radiative recombination processes, such as Auger recombination,[47] are represented by k_{other}. As the defect concentration increases for the crystal grown at 900°C, k_{defect} and ultimately k_{nx} significantly result in PL intensity quenching. TMDCs grown by CVD feature many chalcogen vacancies because chalcogenides are highly volatile, thus making them extremely susceptible to chalcogen deficiencies.[47] The S vacancies are found to be the most common point defects in MoS$_2$ grown by CVD, and they have the ability to introduce localized donor states with energies that were 0.3 eV below the conduction band minimum and 0.2 eV above the valence band minimum within the bandgap.[30] The bandgaps of the direct-gap semiconductor monolayer MoS$_2$ are located at the K and K′ points of the Brillouin zone. In the absence of charged impurities, short-range defects, S vacancies, or trapped charges[47] at the interface between MoS$_2$ and oxide dielectrics, the majority of excited electrons in MoS$_2$ grains shift to the lower states. However, in a situation of localized defects (Fig. 4e), produces a continuum of states. Within a diffusion length of the edge of the defect, the trap will draw in electrons and holes, causing them to non-radiatively recombine via the continuum of states to quench the PL intensity. The photoluminescence results at low laser intensity and low temperature show that the defect level is present around 1.65 eV.

Since doping typically alters the position of the Raman A$_{1g}$ mode, the upshift of the Raman A$_{1g}$ mode seen in the MoS$_2$ crystals grown at 900°C confirms this claim.

Furthermore, an investigation employing X-ray photoelectron spectroscopy is used to investigate the surface chemical states of Mo and S in our morphologically identical MoS$_2$ crystals grown at various temperatures to substantiate the findings of sulfur vacancies. Further, the results in Fig. 5 show that Mo is present in two distinct chemical environments across all samples. In as-grown MoS$_2$ crystals, Mo is found to exist in two different oxidation states, Mo^{4+} and Mo^{6+}, which correspond to the Mo-S and Mo-O bonding conditions.[48,49] The Mo:S ratio is found to be approximately 1:1.83 ± 0.13 (750°C), 1:1.8056 ± 0.31 (800°C), 1:1.1.922 ± 0.32 (850°C), and 1:1.6173 ± 0.13 (900°C). This indicates the change in the stoichiometry of MoS$_2$ crystals grown at different temperatures. The amount of sulfur precursor placed in the CVD growth tube is the same at each growth temperature, but the variation in the stoichiometry of MoS$_2$ suggests that the growth temperature played a role in the Mo:S ratio. According to the findings, MoS$_2$ crystals grown at 900°C are found to have more anionic vacancies than crystals grown at other temperatures. At the higher growth temperatures, the results indicate that extra charges are introduced by the sulfur vacancies and the extra sulfur screens the formation of excitons. It has been found that Mo d$_z^2$ states contribute to the conduction band minimum (CBM) and valence band maximum (VBM) at the K point, while Mo d$_{z2}$ and S p states dominate the CBM at K-Γ and the VBM at Γ.[50] It is possible that the change in the sulfur ratio affected the VBM at Γ, thus quenching the PL efficiency. Fewer anionic vacancies are created in our case than in other techniques such as thermal annealing or electron beam irradiation because the intensity of bound excitons (X$_b$) is lower.

Conclusions

The growth of MoS_2 at different temperatures while maintaining similar morphology is successfully demonstrated. To explore the structural defects in MoS_2 produced by CVD, low-temperature, variable laser intensity, and low laser intensity PL measurements are carried out. Our experimental results suggest that crystals grown at higher temperature (900°C) are prone to sulfur vacancies. The Mo:S ratio determined by XPS shows lower sulfur concentration in crystals produced at 900°C. The growth temperature of 850°C exhibits higher quality crystals. Experimental evidence shows that the anionic vacancies act as defect sites to modulate MoS_2 optical bandgap in a way that causes a new peak to appear below it. These bound excitons are produced as a result of localizing excitons at the defect sites. Our work provides an effective way to grow these crystals at higher temperatures and achieve tunable electronic and optical properties of MoS_2, and also provides a path to grow different TMDC layers and their heterostructures at higher growth temperatures.

References

1. K.S. Novoselov, D. Jiang, F. Schedin, T.J. Booth, V.V. Khotkevich, S.V. Morozov, and A.K. Geim, Two-dimensional atomic crystals. *Proc. Natl. Acad. Sci.* 102(30), 10451 (2005).
2. S. Bertolazzi, J. Brivio, and A. Kis, Stretching and breaking of ultrathin MoS₂. *ACS Nano* 5(12), 9703 (2011).
3. R. Fivaz and E. Mooser, Electron-phonon interaction in semiconducting layer structures. *Phys. Rev.* 136(3A), A833 (1964).
4. R. Saito, Y. Tatsumi, S. Huang, X. Ling, and M.S. Dresselhaus, Raman spectroscopy of transition metal dichalcogenides. *J. Phys. Condens. Matter* 28(35), 353002 (2016).
5. O. Lopez-Sanchez, D. Lembke, M. Kayci, A. Radenovic, and A. Kis, Ultrasensitive photodetectors based on monolayer MoS₂. *Nat. Nanotechnol.* 8, 497 (2013).
6. Q.H. Wang, K. Kalantar-Zadeh, A. Kis, J.N. Coleman, and M.S. Strano, Electronics and optoelectronics of two-dimensional transition metal dichalcogenides. *Nat. Nanotechnol.* 7(11), 699 (2012).
7. S.Z. Butler, S.M. Hollen, L. Cao, Y. Cui, J.A. Gupta, H.R. Gutiérrez, T.F. Heinz, S.S. Hong, J. Huang, A.F. Ismach, and E. Johnston-Halperin, Progress, challenges, and opportunities in two-dimensional materials beyond graphene. *ACS Nano* 7(4), 2898 (2013).
8. S. Bertolazzi, D. Krasnozhon, and A. Kis, Nonvolatile memory cells based on MoS₂/graphene heterostructures. *ACS Nano* 7(4), 3246 (2013).
9. T. Shen, F. Li, L. Xu, Z. Zhang, F. Qiu, Z. Li, and J. Qi, High mobility monolayer MoS₂ transistors and its charge transport behavior under E-beam irradiation. *J. Mater. Sci.* 55(29), 14315 (2020).
10. R. Ganatra and Q. Zhang, Few-layer MoS₂: a promising layered semiconductor. *ACS Nano* 8(5), 4074 (2014).
11. D.Y. Qiu, H. Felipe, and S.G. Louie, Optical spectrum of MoS₂: many-body effects and diversity of exciton states. *Phys. Rev. Lett.* 111(21), 216805 (2013).
12. D. Xiao, G.B. Liu, W. Feng, X. Xu, and W. Yao, Coupled spin and valley physics in monolayers of MoS₂ and other group-VI dichalcogenides. *Phys. Rev. Lett.* 108(19), 196802 (2012).
13. K.F. Mak, K.L. McGill, J. Park, and P.L. McEuen, The valley Hall effect in MoS₂ transistors. *Science* 344(6191), 1489 (2014).
14. Y. Wang, C. Cong, C. Qiu, and T. Yu, Raman spectroscopy study of lattice vibration and crystallographic orientation of monolayer MoS₂ under uniaxial strain. *Small* 9(17), 2857 (2013).
15. X. Zhang, X.F. Qiao, W. Shi, J.B. Wu, D.S. Jiang, and P.H. Tan, Phonon and Raman scattering of two-dimensional transition metal dichalcogenides from monolayer, multilayer to bulk material. *Chem. Soc. Rev.* 44(9), 2757 (2015).
16. K. He, C. Poole, K.F. Mak, and J. Shan, Experimental demonstration of continuous electronic structure tuning via strain in atomically thin MoS₂. *Nano Lett.* 13(6), 2931 (2013).
17. Z. Li, Y. Lv, L. Ren, J. Li, L. Kong, Y. Zeng, Q. Tao, R. Wu, H. Ma, B. Zhao, and D. Wang, Efficient strain modulation of 2D materials via polymer encapsulation. *Nat. Commun.* 11(1), 1 (2020).
18. T. Li, Ideal strength and phonon instability in single-layer MoS₂. *Phys. Rev. B* 85(23), 235407 (2012).
19. M. Hosseini, M. Elahi, M. Pourfath, and D. Esseni, Strain induced mobility modulation in single-layer MoS₂. *J. Phys. D Appl. Phys.* 48(37), 375104 (2015).
20. S. Yu, H.D. Xiong, K. Eshun, H. Yuan, and Q. Li, Phase transition, effective mass and carrier mobility of MoS₂ monolayer under tensile strain. *Appl. Surf. Sci.* 325, 27 (2015).
21. X. Xu, C. Wang, W. Xiong, Y. Liu, D. Yang, X. Zhang, and J. Xu, Strain regulated interlayer coupling in WSe₂/WS₂ heterobilayer. *Nanotechnology* 33(8), 085705 (2021).
22. H.J. Conley, B. Wang, J.I. Ziegler, R.F. Haglund Jr., S.T. Pantelides, and K.I. Bolotin, Bandgap engineering of strained monolayer and bilayer MoS₂. *Nano Lett.* 13(8), 3626 (2013).
23. R. Sahu, D. Radhakrishnan, B. Vishal, D.S. Negi, A. Sil, C. Narayana, and R. Datta, Substrate induced tuning of

compressive strain and phonon modes in large area MoS$_2$ and WS$_2$ van der Waals epitaxial thin films. *J. Cryst. Growth* 470, 51 (2017).

24. E. Scalise, M. Houssa, G. Pourtois, V. Afanas'ev, and A. Stesmans, Strain-induced semiconductor to metal transition in the two-dimensional honeycomb structure of MoS$_2$. *Nano Res.* 5, 43 (2012).

25. M. Ghorbani-Asl, S. Borini, A. Kuc, and T. Heine, Strain-dependent modulation of conductivity in single-layer transition-metal dichalcogenides. *Phys. Rev. B* 87(23), 235434 (2013).

26. S.B. Desai, G. Seol, J.S. Kang, H. Fang, C. Battaglia, R. Kapadia, J.W. Ager, J. Guo, and A. Javey, Strain-induced indirect to direct bandgap transition in multilayer WSe$_2$. *Nano Lett.* 14(8), 4592 (2014).

27. W.H. Chae, J.D. Cain, E.D. Hanson, A.A. Murthy, and V.P. Dravid, Substrate-induced strain and charge doping in CVD-grown monolayer MoS$_2$. *Appl. Phys. Lett.* 111(14), 143106 (2017).

28. A. Koma, Van der Waals epitaxy—a new epitaxial growth method for a highly lattice-mismatched system. *Thin Solid Films* 216(1), 72 (1992).

29. B. Chakraborty, A. Bera, D.V.S. Muthu, S. Bhowmick, U.V. Waghmare, and A.K. Sood, Symmetry-dependent phonon renormalization in monolayer MoS$_2$ transistor. *Phys. Rev. B* 85(16), 161403 (2012).

30. S. Tongay, J. Suh, C. Ataca, W. Fan, A. Luce, J.S. Kang, J. Liu, C. Ko, R. Raghunathanan, J. Zhou, and F. Ogletree, Defects activated photoluminescence in two-dimensional semiconductors: interplay between bound, charged and free excitons. *Sci. Rep.* 3(1), 1 (2013).

31. A. Inoue, T. Komori, and K.I. Shudo, Atomic-scale structures and electronic states of defects on Ar$_+$−ion irradiated MoS$_2$. *J. Electron Spectrosc. Relat. Phenom.* 189, 11 (2013).

32. Y. Gong, S. Ye, S. Lei, G. Shi, Y. He, J. Lin, X. Zhang, R. Vajtai, S.T. Pantelides, W. Zhou, and B. Li, Synthesis of millimeter-scale transition metal dichalcogenides single crystals. *Adv. Func. Mater.* 26(12), 2009 (2016).

33. S. Barja, S. Refaely-Abramson, B. Schuler, D.Y. Qiu, A. Pulkin, S. Wickenburg, H. Ryu, M.M. Ugeda, C. Kastl, C. Chen, C. Hwang, A. Schwartzberg, S. Aloni, S.K. Mo, D. Frank Ogletree, M.F. Crommie, O.V. Yazyev, S.G. Louie, J.B. Neaton, and A. Weber-Bargioni, Identifying substitutional oxygen as a prolific point defect in monolayer transition metal dichalcogenides. *Nat. Commun.* 10(1), 3382 (2019).

34. S. Geng, W. Yang, Y. Liu, and Y. Yu, Engineering sulfur vacancies in basal plane of MoS$_2$ for enhanced hydrogen evolution reaction. *J. Catal.* 391, 91 (2020).

35. A. Zak, Y. Feldman, V. Alperovich, R. Rosentsveig, and R. Tenne, Growth mechanism of MoS$_2$ fullerene-like nanoparticles by gas-phase synthesis. *J. Am. Chem. Soc.* 122(45), 11108 (2000).

36. J.D. Cain, F. Shi, J. Wu, and V.P. Dravid, Growth mechanism of transition metal dichalcogenide monolayers: the role of self-seeding fullerene nuclei. *ACS Nano* 10(5), 5440 (2016).

37. Y. Feldman, E. Wasserman, D.J. Srolovitz, and R. Tenne, High-rate, gas-phase growth of MoS$_2$ nested inorganic fullerenes and nanotubes. *Science* 267(5195), 222 (1995).

38. S. Kataria, S. Wagner, T. Cusati, A. Fortunelli, G. Iannaccone, H. Pandey, G. Fiori, and M.C. Lemme, Growth-induced strain in chemical vapor deposited monolayer MoS$_2$: experimental and theoretical investigation. *Adv. Mater. Interfaces* 4(17), 1700031 (2017).

39. W.K. Burton and N. Cabrera, Crystal growth and surface structure. Part I. *Discuss. Faraday Soc.* 5, 33 (1949).

40. K.M. McCreary, A.T. Hanbicki, S.V. Sivaram, and B.T. Jonker, A-and B-exciton photoluminescence intensity ratio as a measure of sample quality for transition metal dichalcogenide monolayers. *APL Mater.* 6(11), 111106 (2018).

41. M. Velicky, A. Rodriguez, M. Bousa, A.V. Krayev, M. Vondracek, J. Honolka, and O. Frank, Strain and charge doping fingerprints of the strong interaction between monolayer MoS$_2$ and gold. *J. Phys. Chem. Lett.* 11(15), 6112 (2020).

42. A. Michail, N. Delikoukos, J. Parthenios, C. Galiotis, and K. Papagelis, Optical detection of strain and doping inhomogeneities in single layer MoS$_2$. *Appl. Phys. Lett.* 108, 173102 (2016).

43. H. Kim, T. Lee, H. Ko, S.M. Kim, and H. Rho, Influence of chemical treatment on strain and charge doping in vertically stacked monolayer–bilayer MoS$_2$. *Appl. Phys. Lett.* 117, 202104 (2020).

44. K. Ponnusamy, S. Durairaj, and S. Chandramohan, Effect of growth temperature on the morphology control and optical behavior of monolayer MoS$_2$ on SiO$_2$ substrate. *J. Mater. Sci. Mater. Electron.* 33(12), 9549 (2022).

45. T.L.K.Z. Schmidt, K. Lischka, and W. Zulehner, Excitation-power dependence of the near-band-edge photoluminescence of semiconductors. *Phys. Rev. B* 45(16), 8989 (1992).

46. S. Poduri, M. Dutta, and M. Stroscio, Characterization of CdS nanowires self-assembled in a nanoporous alumina template. *J. Electr. Mater.* 43, 3979 (2014).

47. A. Zafar, H. Nan, Z. Zafar, Z. Wu, J. Jiang, Y. You, and Z. Ni, Probing the intrinsic optical quality of CVD grown MoS$_2$. *Nano Res.* 10(5), 1608 (2017).

48. X. Wei, Z. Yu, F. Hu, Y. Cheng, L. Yu, X. Wang, M. Xiao, J. Wang, X. Wang, and Y. Shi, Mo-O bond doping and related-defect assisted enhancement of photoluminescence in monolayer MoS$_2$. *AIP Adv.* 4(12), 123004 (2014).

49. S. Durairaj, K. Ponnusamy, N.B. Shinde, S.K. Eswaran, V. Asokan, J.B. Park, and S. Chandramohan, Oxygen-driven growth regulation and defect passivation in chemical vapor deposited MoS$_2$ monolayers. *Cryst. Growth Des.* 21(12), 6793 (2021).

50. F. Wang, J. Wang, S. Guo, J. Zhang, Z. Hu, and J. Chu, Tuning coupling behavior of stacked heterostructures based on MoS$_2$, WS$_2$, and WSe$_2$. *Sci. Rep.* 7(1), 1 (2017).